Filament Recycling and Sustained Contractile Flows in an Actomyosin Cortex

William M McFadden[1], Patrick M McCall[2], Edwin M Munro[3,*]

1 Biophysical Sciences Program, University of Chicago, Chicago, IL, USA
2 Department of Physics, University of Chicago, Chicago, IL, USA
3 Department of Molecular Genetics and Cell Biology, University of Chicago, Chicago, IL, USA

* emunro@uchicago.edu

Abstract

Fill in abstract later.

Author Summary

In this paper, we develop and analyze a minimal model for 2D active networks based on the cortical cytoskeleton of eukaryotic embryos. Our model introduces a series of coarse-grained approximations for simultaneous comparison of cross-link stress dissipation, myosin driven active stress generation and a form of rapid filament turnover we term *filament recycling*. We generate computational simulations based on the model and demonstrate that our minimal assumptions are sufficient to drive network contraction and to set up steady state flow profiles such as those found in the cortex of developing embryos and migrating cells. Our analysis sheds insight on potential microscopic control parameters governing broad qualitative differences in 2D active networks.

Introduction

   Cortical flow is a fundamental and ubiquitous form of cellular deformation that underlies cell polarization, cell division, cell crawling and multicellular tissue morphogenesis [Bray and White, 1988, Hird and White, 1993]. These flows arise within the actomyosin cortex, a thin layer of cross-linked actin filaments and myosin motors that lies just beneath the plasma membrane [Salbreux et al., 2012]. The active forces that drive cortical flows are thought to be generated by myosin motors pulling against individual actin filaments [Munro et al., 2004]. These forces must be integrated within cross-linked networks to build macroscopic contractile stress. At the same time, cross-linked networks resist deformation and this resistance must be dissipated by network remodeling to allow macroscopic network deformation and flow. How force production and dissipation depend on motor activity, network architecture and remodeling remains poorly understood.
   Current models for cortical flow rely on coarse-grained descriptions of actomyosin networks as active fluids, whose motions are driven by gradients of active contractile stress and opposed by an effectively viscous resistance [Mayer et al., 2010]. In these

models, gradients of active stress are assumed to reflect spatial variation in motor activity and viscous resistance is assumed to reflect the internal dissipation of elastic resistance due to local remodeling of filaments and/or cross-links [Bois et al., 2011]. A key virtue of these models is that their behavior is governed by a few parameters (active stress and effective viscosity). By coupling an active fluid description to simple kinetic models for network assembly and disassembly and making active stress and effective viscosity depend on e.g network density and turnover rates, it is possible to capture phenomenological descriptions of cortical flow. Models based on this active fluids description can successfully reproduce spatiotemporal dynamics of cortical flow observed during polarization [Mayer et al., 2010], cell division [Turlier et al., 2014, Salbreux et al., 2009], cell motility [Keren et al., 2009, Marchetti et al., 2013] and tissue morphogenesis [Heisenberg and Bellaïche, 2013].

However, to understand how cells exert physiological control over cortical deformation and flow, or to build and tune networks with desired properties *in vitro*, it is essential to connect this coarse-grained description to the microscopic origins of force generation and dissipation within cross-linked actomyosin networks. Both active stress and effective viscosity depend sensitively on microscopic parameters including densities of filaments, motors and cross-links, force-dependent motor/filament interactions, cross-link dynamics and network turnover rates. Thus a key challenge is to understand how tuning these microscopic parameters controls the dynamic interplay between active force generation and passive relaxation to control macroscopic dynamics of cortical flow.

Studies in living cells have documented fluid-like stress relaxation on timescales of 10-100s of seconds [Mayer et al., 2010, Hird and White, 1993, Bray and White, 1988, Hochmuth, 2000, Evans and Yeung, 1989, Bausch et al., 1998]. These modes of stress relaxation are thought to arise both from the transient binding/unbinding of individual cross-links and from the turnover (assembly/disassembly) of actin filaments (ref). Studies of cross-linked and/or bundled actin networks *in vitro* suggest that cross-link unbinding may be sufficient to support viscous relaxation (creep) on very long timescales [Wachsstock et al., 1994, Lieleg et al., 2008, Lieleg et al., 2009, Yao et al., 2011, Liu et al., 2007], but is unlikely to explain the rapid large scale cortical deformation and flow observed in living cells. It has been proposed in the field that rapid actin turnover must play a significant role as well. Indeed, photokinetic and single molecule imaging studies studies reveal rapid turnover of cortical actin filaments in living cells on timescales of 10-100 seconds [Robin et al., 2014]. Previous theoretical models have explored the dependence of stress relaxation on cross-link binding and unbinding analytically [Broedersz et al., 2010, Müller et al., 2014] and others have explicitly modeled reversible cross-linking in combination with complex mechanics of filament bundles [Kim et al., 2011, Lieleg et al., 2009, Lieleg and Bausch, 2007], leading to complex viscoelastic stress relaxation. However, until very recently [Mak et al., 2016] very little attention has been paid to actin turnover as mechanism of stress relaxation.

Recent work has also begun to reveal insights into mechanisms that govern active stress generation in disordered actomyosin networks. In vitro studies have confirmed that local interactions among actin filaments and myosin motors are sufficient to drive macroscopic contraction of disordered networks [Murrell and Gardel, 2012]. Theoretical studies suggest that asymmetrical compliance of actin filaments (stiffer under extension than compression) and spatial differences (dispersion) in motor activity are sufficient conditions for contraction in one [Lenz et al., 2012] and two [Lenz, 2014] dimensional networks, although other routes to contractility may also exist [Lenz, 2014]. Further work has explored how modulation of network architecture, cross-link dynamics and motor density, activity and assembly state can shape rates and patterns of network deformation [Köhler and Bausch, 2012, Alvarado et al., 2013, Banerjee and Marchetti,

2011] or network rheology [Liverpool et al., 2009, Koenderink et al., 2009].

Significantly, *in vitro* models for disordered actomyosin networks have used stable actin filaments, and these networks support only transient contraction, either because of network collapse [Alvarado et al., 2013], or buildup of elastic resistance [Murrell and Gardel, 2014], or because network rearrangements (polarity sorting) dissipate the potential to generate contractile force [Nedelec et al., 1997, Surrey et al., 2001]. This suggests that continuous turnover of actin filaments may play a key role in allowing sustained deformation and flow. Recent theoretical and modeling studies have begun to explore how this could work [Hiraiwa and Salbreux, 2015, Mak et al., 2016, Zumdieck et al., 2007], and to explore dynamic behaviors that can emerge in contractile material with turnover [Dierkes et al., 2014]. However, there is much to learn about how the buildup and maintenance of contractile force during continuous deformation and flow depends on the local interplay of network architecture, motor activity and filament turnover.

The goal of this work is to build a computational bridge between the microscopic description of cross-linked actomyosin networks and the coarse grained macroscopic description of an active fluid. We seek to capture the essential microscope features (dynamic cross-links, active motors and semi flexible actin filaments with asymmetric compliance and continuous filament recycling), but in a way that is sufficiently simple to allow systematic exploration of how parameters that govern network deformation and flow in an active fluid theory depend on microscopic parameters. To this end, we introduce several coarse-grained approximations into our representation of filament networks. First, we represent semi-flexible actin filaments as simple springs with asymmetric compliance (stronger in extension than compression). Second, we replace dynamic binding/unbinding of elastic cross-links with a coarse-grained representation in terms of molecular friction [Vanossi et al., 2013, Spruijt et al., 2010, Filippov et al., 2004], such that filaments can slide past each other against a constant fictional resistance. Third, we used a similar scheme to introduce active motors at filament crossover points with a simple linear force/velocity relationship, and we introduce dispersion of motor activity by making only a subset of filament overlaps active [Banerjee et al., 2011]. Finally, we model filament turnover by regularly resetting a subset of filaments to a new unstrained position. Importantly, these simplification allows us to extend our single polymer models to dynamical systems of larger network models for direct comparison between theory and modeling results. This level of coarse graining will therefore make it easier to understand classes of behavior for varying compositions of cross-linked filament networks. In addition, it allows us to compute a new class of numerical simulations efficiently, which gives us concrete predictions for behaviors in widely different networks with measurable dependencies on molecular details.

Models

Our motivation is to model essential microscope features of cross-linked actomyosin networks (semi flexible actin filaments with asymmetric compliance, dynamic cross-links, active motors and and continuous filament recycling), in a way that is simple enough to allow systematic exploration of how tuning these microscopic features controls macroscopic network deformation and flow. We focus on 2D networks for computational tractability and because they capture a reasonable approximation of the quasi-2D cortical actomyosin networks that govern flow and deformation in many eukaryotic cells [Mayer et al., 2010, Chugh et al., 2016], or the quasi-2D networks used in recent in vitro studies [Murrell and Gardel, 2012, Sanchez et al., 2012].
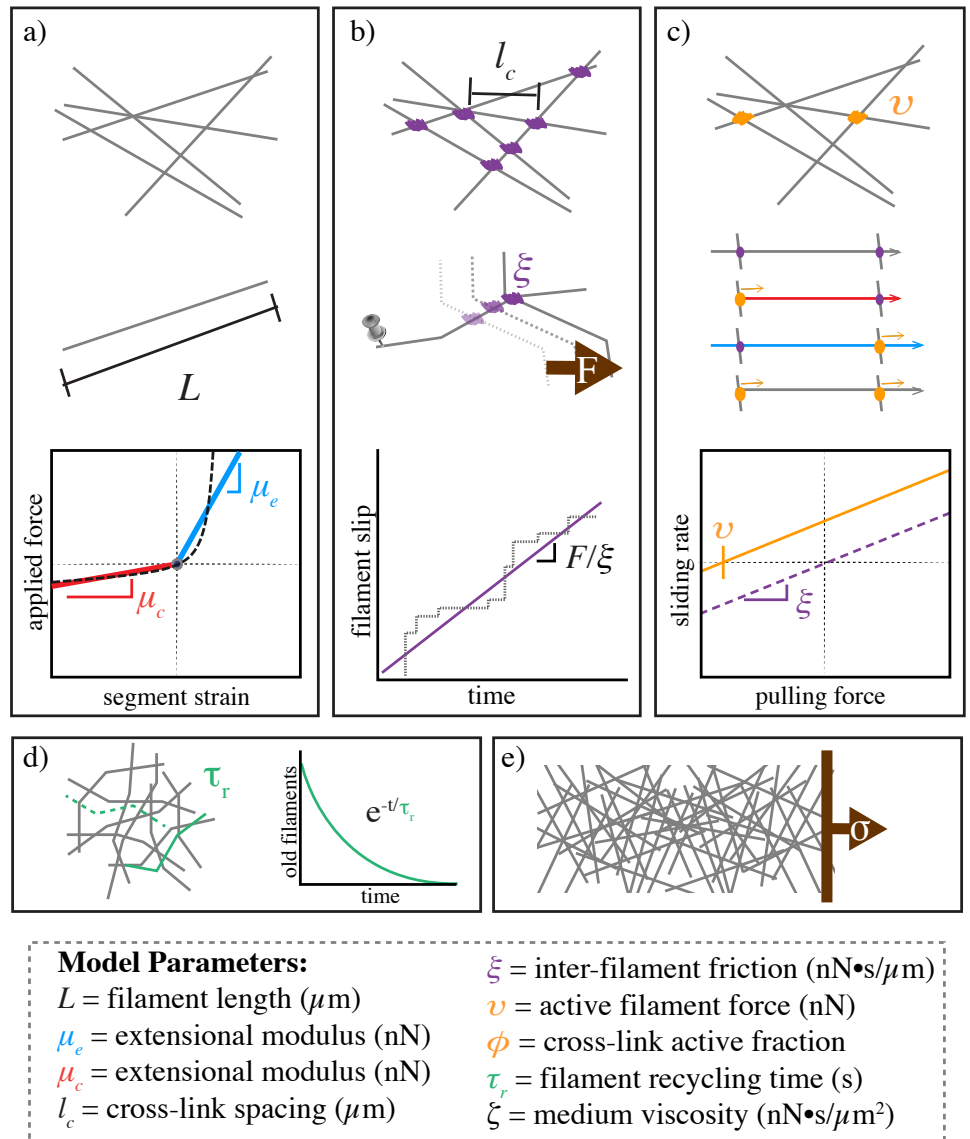
Figure 1. Schematic of modeling framework. a) Asymmetric filament compliance.Filaments have smaller spring constant for compression than for extension. b) Cross-link slip. Cross-links are coupled by an effective drag, such that their relative motion is proportional to any applied force. c) Motor activity. Filament activity manifests as a basal sliding rate even in the absence of an external force. Fractional activity. Only a subset of filament cross-links are active, resulting in differential force exertion along the filament. d) Filament recycling. Filaments are turned over at a constant rate, leading to a refreshing in the strain state of all filaments after a characteristic timescale. e) Applied stress. In simulations with passive cross-links, and external stress is applied as force filed acting on a fixed spatial domain.

Asymmetric filament compliance

We model individual filaments as chains of springs with relaxed length l_s. Filaments can therefore be represented as a sequence of nodes with positions $\mathbf{x_i}$ and nearest neighbor

force interactions, $\mathbf{F_i^\mu}$, of the form

$$\mathbf{F_{i,i+1}^\mu} = \mu \frac{|\mathbf{x_{i+1}} - \mathbf{x_i}| - l_s}{l_s} \left(\frac{\mathbf{x_{i+1}} - \mathbf{x_i}}{l_s} \right) \tag{1}$$

where the modulus, μ, is a composite quantity representing both filament and cross-linker compliance in a manner similar to a proposed effective medium theory [Broedersz et al., 2009]. To model asymmetric filament compliance, we assign the modulus μ, a different value depending on whether $(|\mathbf{x_{i-1}} - \mathbf{x_i}| - l_s)/l_s$ (the strain) is greater or less than 0. In the limit of highly rigid cross-links and flexible filaments, our model reduces to the pure semi-flexible filament models of [Head et al., 2003, Wilhelm and Frey, 2003]. In the opposite regime of nearly rigid filaments and highly flexible cross links, our method is still largely similar to the model of [Broedersz et al., 2009] in small strain regimes before any nonlinear cross link stiffening. In a departure from those models, we assume here that the magnitude of the force on interior cross-links is the same as those on the exterior. This approach ignores the variation in strain on these two sets of cross-links as addressed in [Broedersz et al., 2009], but we choose to ignore this variation in favor of an approximated, global mean approach.

Because we are dealing with semi-flexible filaments we also introduce a bending modulus between our filament segments such that the restoring force is proportional to the angle between the filament segments and points in the direction orthogonal to the filament direction, $\mathbf{u_i} = (\mathbf{x_{i-1}} - \mathbf{x_i})/|\mathbf{x_{i-1}} - \mathbf{x_i}|$.

$$\mathbf{F_{i-1,i,i+1}^\kappa} = \frac{\kappa}{l_s} acos \left(\frac{(\mathbf{x_{i+1}} - \mathbf{x_i}) \cdot (\mathbf{x_{i-1}} - \mathbf{x_i})}{|\mathbf{x_{i+1}} - \mathbf{x_i}| \cdot |\mathbf{x_{i-1}} - \mathbf{x_i}|} \right) \mathbf{u_{i\perp}} \tag{2}$$

However, this introduces another mode of asymmetric compliance since filaments under compression are able to bend outward at their centers. For this reason, in the majority of the work in this paper, we have selected to set $l_s = L$ to simplify away the dependence on bending driven asymmetries. We show in our supplemental figures (TBA) that the major points of the paper are still valid when we set $l_s < L$ under the condition that $\kappa/l_s \gg \mu_c$. Therefore, in the majority of the paper we limit our focus to filaments that are constrained not to bend.

Together these forces combine into a single term denoting all the internal forces of the filament mechanics.

$$\mathbf{F_i^{int}} = \mathbf{F_{i-1,i}^\mu} + \mathbf{F_{i,i+1}^\mu} + \mathbf{F_{i-1,i,i+1}^\kappa} - \mathbf{F_{i-2,i-1,i}^\kappa} - \mathbf{F_{i,i+1,i+2}^\kappa} \tag{3}$$

Drag-like coupling between overlapping filaments

Previous models represent cross-linkers as elastic connections between pairs of points on neighboring filaments that appear and disappear with either fixed or force-dependent probabilities [Kim et al., 2011, Broedersz et al., 2009]. Here, we introduce a simpler coarse-grained model for dynamic cross-links by replacing many transient elastic interactions with an effective drag-like coupling between every pair of overlapping segments.

$$\mathbf{F_{i-1,i}^\xi} = \xi \sum_j \frac{l_s - |s_{ij} - s_i|}{l_s} (\mathbf{v_{i-1,i}} - \mathbf{v_{j-1,j}}) \tag{4}$$

where $\mathbf{v_{n-1,n}}$ represent the average velocity of the filament segment stretching between filament node $n - 1$ and node n, and the sum is taken over all filament segments such that the segment from node $j - 1$ to node j intersects the segment from $i - 1$ to i at the location s_{ij}.

$$\mathbf{F_i^{coup}} = \mathbf{F_{i-1,i}^\xi} + \mathbf{F_{i,i-1}^\xi} \tag{5}$$

This model assumes a linear relation between applied force and the velocity difference between attached segments. This drag-like coupling has been shown to be an adequate approximation in the case of ionic cross-linking of actin [Ward et al., 2015, Chandran and Mofrad, 2010], and can be found in the theoretical basis of force-velocity curves for myosin bound filaments [Banerjee et al., 2011]. Although non-linearities can arise through force dependent detachment kinetics and/or non-linear force extension of cross-links, we assume that inhomogeneities from non-linear effects are of second or higher order. With this assumption, the motion of filaments can be described by a deterministic dynamical equation of the form

$$0 = -l_s \zeta \mathbf{v_i} - \mathbf{F_i^{coup}} + \mathbf{F_i^{int}} \tag{6}$$

Here, the first term in the integral is the filament's intrinsic drag through its embedding fluid, ζ, while the second comes from the drag-like coupling between filaments, ξ.

Active coupling for motor driven filament interactions

To add motor activity we select a subset of cross-linked points and impart an additional force of magnitude υ directed in the orientations of the individual filaments, $\mathbf{u_i} = (\mathbf{x_{i-1}} - \mathbf{x_i})/|\mathbf{x_{i-1}} - \mathbf{x_i}|$. This leads to a modification of the equation of motion to

$$\mathbf{F_{i-1,i}^{\upsilon}} = \upsilon \mathbf{u_i} \sum_j \frac{l_s - |s_{ij} - s_i|}{l_s} q_{ij} \tag{7}$$

where q_{ij} can be 0 or 1 depending on whether there is an "active" cross-linker at this location. In this formulation, only at the subset of points where $q_{ij} = 1$ will there be a force imparted. In our simulations we let q_{ij} be selected randomly such that $\bar{q} = \phi$, where $\bar{q}$ indicates the mean of q.

Finally, for each active force, $\mathbf{F_j^{act}}$, imparted by filament j, we must also impart the opposite force onto the filament between i and $i + 1$ as well. Therefore, the entire equation for activity will appear as

$$\mathbf{F_i^{act}} = \mathbf{F_{i-1,i}^{\upsilon}} + \mathbf{F_{i,i+1}^{\upsilon}} - \sum_j \mathbf{F_{j-1,j}^{\upsilon}} q_{ij} \tag{8}$$

This will leave us with a full equation of motion given by the sum of each of the parts defined above.

$$0 = -L \zeta \mathbf{v_i} - \mathbf{F_i^{coup}} + \mathbf{F_i^{int}} + \mathbf{F_i^{act}} \tag{9}$$

2D network formation

We used a mikado model approach [Unterberger and Holzapfel, 2014] to initialize a minimal network of connected unstressed linear filaments in a rectangular 2D domain. We generate 2D networks of these semi-flexible filaments by laying down straight lines of length, L, with random position and orientation. We then assume that overlapping filaments become cross-linked at their points of overlap. Although real cytoskeletal networks may form with non-negligible anisotropy, for simplicity, we focus on isotropically initialized networks. We define the density using the average distance between cross-links along a filament, l_c. A simple geometrical argument can then be used to derive the number of filaments filling a domain as a function of L and l_c [Head et al., 2003]. Here, we use the approximation that the number of filaments needed to tile a rectangular domain of size $D_x \times D_y$ is $2D_x D_y / L l_c$, and that the length density is

therefore simply, $2/l_c$. In the absence of cross-link slip, we expect the network to form a connected solid with a well defined elastic modulus [Head et al., 2003, Wilhelm and Frey, 2003].

External applied stress

We can model our active networks as a coupled system of differential equations satisfying 9. However, to probe the passive response of the network, we also wish to incorporate externally applied stresses. Although the general passive mechanical response of this system may be very complex, we focus our attention on low frequency deformations and the steady-state creep response of the system to an applied stress. To do this we introduce a fixed stress, σ along a fixed domain at one edge of the network. The stress is applied via individual forces to the filaments lying within a patch of size D_w such that the sum of individual forces is equal to the applied stress times the height of the domain. These forces points in the direction, $\hat{\mathbf{x}}$, producing an extension of the patch. The region of applied stress does not move as the network deforms, allowing us to more easily focus our attention on a fixed sized domain.

Finally, we add a 0 velocity constraint at the other edge of our domain of interest. We assume that our network is in the "dry," low Reynold's number limit, where inertial effects are so small that we can equate our total force to 0. Therefore, we have a dynamical system of wormlike chain filaments satisfying

$$0 = -L\zeta\mathbf{v_i} - \mathbf{F_i^{coup}} + \mathbf{F_i^{int}} + \mathbf{F_i^{act}} + \sigma\hat{\mathbf{u}}(\mathbf{x_i}) \tag{10}$$

subject to constraints such that $\mathbf{v_i}(\mathbf{x})$ is 0 with $x = 0$. This results in an implicit differential equation for filament segments which can be discretized and integrated in time to produce a solution for the motion of the system.

Modeling filament turnover

In living cells, actin filament assembly is governed by multiple factors that control nucleation, elongation and filament branching. Likewise filament disassembly is governed by multiple factors that promote filament severing and monomer dissociation at filament ends. Here, we focus on a lowest order model for filament recycling in which entire filaments appear with a fixed rate per unit area, k_{app} and disappear at a rate $k_{diss}\rho$, where ρ is a filament density. With this assumption, in the absence of network deformation, the density of filaments will equilibrate to a steady state density, k_{app}/k_{diss}, with time constant $\tau_r = 1/k_{diss}$. In deforming networks, the density will be set by a competition between strain thinning ($\gamma > 0$) or thickening ($\gamma < 0$), and density equilibration via turnover. To implement this assumption, at fixed time interval $\tau_s < 0.01 \cdot \tau_r$ (i.e. 1% of the equilibration time), we selected a fraction, τ_s/τ_r, of existing filaments (i.e. less than 1% of the total filaments) for degradation. We then generated a fixed number of new unstrained filaments $k_{app}\tau_s D_x D_y$ at random positions and orientations within the original domain. We refer to this continuous turnover as filament recycling, to $k_{diss} = 1/\tau_r$ as the recycling rate, and to τ_r as the recycling time.

Simulation methods

Details of our simulation approach can be found in the Appendix. Briefly, equations 1,5,7 and 10 define a coupled system of ordinary differential equations for the velocities of the endpoints of filament segments, $\dot{\mathbf{x}}$. These equations are coupled by the effective cross-link friction on segment overlap points, yielding a system of the form:

$$\mathbf{A} \cdot \dot{\mathbf{x}} = \mathbf{f}(\mathbf{x}) \tag{11}$$

where $\mathbf{A}$ represents a coupling matrix between endpoints of filaments that overlap, and $\mathbf{f}(\mathbf{x})$ is the spring force between pairs of filament segment endpoints. We numerically integrate this system of equations to find the time evolution of the positions of all filament endpoints. We generate a network of filaments with random positions and orientations as described above within a domain of size D_x by D_y. For all simulations, we imposed periodic boundaries in the y-dimension. To impose an extensional stress, we constrained all filament segment endpoints within a fixed distance $0.05 \cdot D_x$ from the left edge of the domain to be non-moving, then we imposed a rightwards force on all segment endpoints within a distance $0.05 \cdot D_x$ from the left edge of the patch. To simulate free contraction, we removed all constraints at boundaries; to assess buildup of contractile stress under isometricc conditions, we pinned both left and right edges of the network as described above.

We smoothed all filament interactions, force fields, and constraints over small regions such that the equations contained no sharp discontinuities. The nominal units for length, force, and time are μm, nN, and s, respectively. We explored parameter space around an estimate of biologically relevant parameter values given in Table 1.

Table 1. Simulation Parameter Values

parameter	symbol	physiological estimate
extensional modulus	μ_e	$1nN$
compressional modulus	μ_c	$0.01nN$
cross-link drag coefficient	ξ	$unknown$
solvent drag coefficient	ζ	$0.0005\frac{nNs}{\mu m^2}$
filament length	L	$5\mu m$
cross-link spacing	l_c	$0.5\mu m$
domain size	$D_x \times D_y$	$20 \times 50 \mu m$

Results and Discussion

We aim to characterize how rates and patterns of cortical flow are shaped by complex dependencies of active stress generation and passive stress dissipation on network architecture, local coupling (active and passive) between filaments and filament recycling. We approached this in three steps: First, we analyzed the passive deformations of cross-linked networks (absent active motors) in response to a constant external force. Then, we analyzed the dynamics of internal stress buildup and dissipation in the same networks, but with active motors, as they contract freely or build force against fixed external boundaries. Finally, we consider the dynamic interplay of internal stress buildup, contraction, and stress relaxation in networks that undergo steady state flow in response to spatial gradients of motor activity.

Filament recycling prevents cortical tearing and modulates the viscous stress relaxation of passive filament networks

Networks with passive cross-links and no filament turnover undergo three stages of deformation in response to an extensional force. To characterize the passive response of a cross-linked filament network in the absence of filament recycling and motor activity, we imposed an external force on the simulated network, and then quantified the mechanical response in terms of internal network stress and network strain as a function of time. Figure 2a shows the typical response of a simulated network. We measured the local velocity of the network at different positions along the axis of deformation as the mean velocity of all filament segments intersecting

that position; we measured the internal network stress at each position by summing the axial component of the tensions on all filament segments intersecting that position, and dividing by network height; finally, we measured network strain rate as the average of all filaments velocities divided by their positions.

During early (not shown) and intermediate (Figure 2b) stages of the deformation, the internal stress (blue) was nearly constant throughout the material while the velocity (orange) increased linearly with distance from the site of network attachment, indicating an approximately uniform deformation (strain) rate throughout the material. Accordingly, we report the network response in terms of time-dependent bulk material stress and strain.

Plotting the bulk stress and strain as a function of time revealed that the deformation occurred in three qualitatively distinct phases (Figure 2a,c). On short timescales the response was viscoelastic, with a rapid buildup of internal stress and a rapid ~exponential approach to a fixed strain, which represents the elastic limit in the absence of cross-link slip predicted by [Head et al., 2003]. On intermediate timescales, the internal stress remained constant while the network continued to deform slowly and continuously with nearly constant strain rate (shown as dashed line in Fig 2c) as filaments slipped past one another against the effective cross-link drag. This linear relationship between strain and time characterizes a material with an effective viscosity, η, given by the ratio of the applied stress to the strain rate. We define the transition time between the fast, viscoelastic phase and the slower, effectively viscous deformation phase as τ_c. Finally, as the network strain approached a critical value ($\sim 30\%$ for the simulation in Figure 2), strain thinning led to decreased network connectivity, local tearing, and acceleration of the network deformation (see inset in Figure 2c), eventually resulting in the highly heterogeneous network structure shown in the t=440s example of Figure 2a.

Network architecture sets the rate and timescales of deformation. To better understand how network architecture and cross-link dynamics control effective viscosity and the timescale for transition to viscous behavior, we systematically varied network parameters (see S1 Table), and measured the elastic modulus, G_0, effective viscosity, η, and transition time, τ_c, in response to a fixed external stress. We observed the transition from a viscoelastic to an effectively viscous phase for the entire range of parameters that we sampled. The elastic limit that we observe during the viscoelastic phase agreed closely with the closed form solution for the elastic modulus $G_0 \sim \mu/l_c$ predicted by a previous model [Head et al., 2003] for networks of semi-flexible filaments with irreversible cross-links (S2 Fig). A simple theoretical analysis (shown in S1 Text) predicts that in the viscous phase, the effective viscosity should be proportional to the cross-link drag coefficient and to the square of the number of cross-links per filament, with a constant of proportionality $\pi/4$. We define this predicted scaling of effective viscoisty as η_c.

$$\eta_c = \frac{\pi}{4}\xi \left(\frac{L}{l_c} - 1 \right)^2 \tag{12}$$

As shown in Figure 3a, our simulations agree well with this prediction for a large range of network parameters. For many linear viscoelastic materials, the ratio of the viscosity, η_c, to the elastic modulus, G_0, is a general indicator of the transition timescale from elastic to viscous behavior [McCrum et al., 1997]. Using our approximations of the elastic modulus and viscosity, we predict a crossover time, $\tau_c \approx L^2\xi/l_c\mu$. By measuring the time at which the strain rate became nearly constant (i.e $\gamma \sim t^n$ with $n > 0.8$) we obtained an estimate of this time for a wide variety of simulation parameters. As shown in Figure 3b, our approximation is in good agreement with the observed transition time,
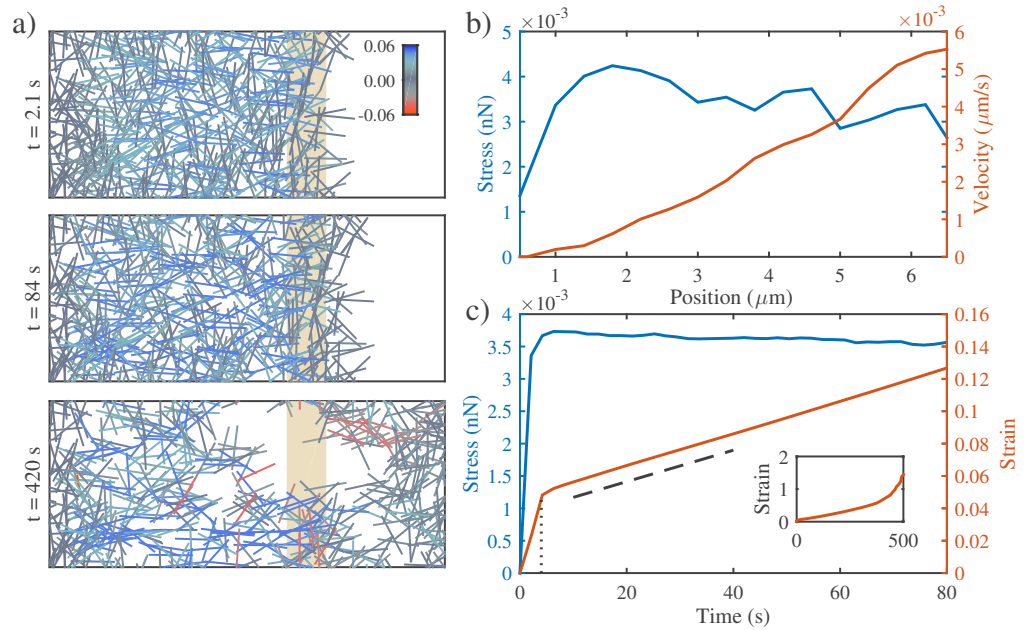
Figure 2. Networks with passive cross-links and no filament turnover undergo three stages of deformation in response to an extensional force. **a)** Three successive time points from a simulation of a $4 \times 6.6\,\mu m$ network deforming under an applied extensional stress of $0.005\,nN/\mu m$ (stress is applied to filaments in the region indicated by the tan bar). Network deforms to a final dimension of $\sim 4 \times 10\,\mu m$. In this and all subsequent figures, filaments are color-coded with respect state of strain (blue = tension, red = compression). Network parameters: $L = 1\,\mu m$, $l_c = 0.3\,\mu m$, $\xi = 100\,nN \cdot s/\mu m$. **b)** Mean filament stress and velocity profiles for the network in (a) at t=88s. Note that the stress is nearly constant and the velocity is nearly linear as predicted for a viscous fluid under extension. **c)** Plots of the mean stress and strain vs time for the simulation in (a), illustrating the three stages of deformation: (i) A fast initial phase accompanies rapid buildup of internal network stress; (ii) after a characteristic time τ_c (indicated by vertical dotted line) the network deforms like a material with a constant effective viscosity, η_c, as indicated by the slope of the dashed line; (iii) at long times, the strain accelerates (see inset) as the network undergoes strain thinning and eventually tears.

indicating that the passive responses of our simulated networks are well represented by effectively linear bulk properties, at least over small strains.

Filament recycling rescues network tearing and modulates effective viscosity. To explore how filament recycling shapes the passive network response to an applied force, we ran a series of simulations with identical filament lengths and network densities and cross-link drag coefficients, while varying the filament recycling time $\tau_r = 1/k_{diss}$. Figure 4a illustrates the results for a particular set of network parameters. In the absence of filament recycling, strain thinning and network tearing lead to a rapid increase in strain rate above a critical strain of $\sim 40\%$.

Progressively decreasing the filament recycling time led to a progressive increase in the rate of network deformation during the effectively viscous phase and an increase in the critical strain at which the network began to tear. As we decreased the recycling time below a critical recycling time (τ_{crit}), the networks began to sustain effectively viscous deformation indefinitely, as shown by the lack of strain thinning in the strain
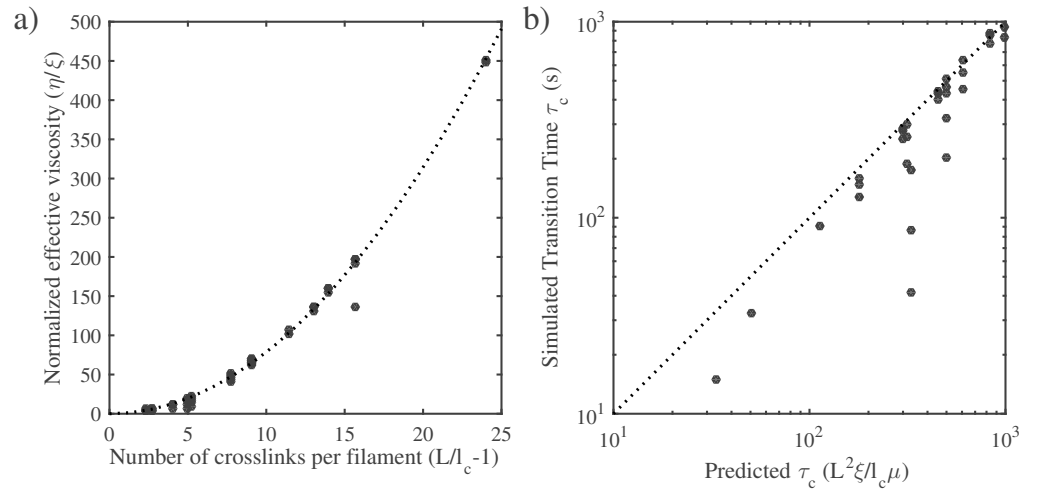
Figure 3. Network architecture sets the rate and timescales of deformation. **a)** The effective viscosity depends on the drag coefficient and the density of the network. Data points are the normalized effective viscosity from simulations (effective viscosity measured in fluid phase divided by the cross link friction coefficient) vs the number of cross links per filament ($L/l_c - 1$). Dotted line indicates the relationship predicted by a simple theory, $\eta_c = \xi(L/l_c - 1)^2$ **b)** The transition to viscous behavior occurs at a characteristic time, τ_c.

profiles of (ANOTHER SUPPLEMENTAL FIGURE). Intuitively, steady state deformation is achieved when the rate of filament depletion by strain thinning is balanced by a sufficiently high rate of filament recycling (i.e. a sufficiently low recycling time). To determine the critical recycling time, we write an equation for the rate of change in filament density ρ, as a function of filament recycling ($k_{app} - k_{diss}\rho$) and strain thinning ($-\dot{\gamma}\rho$). These terms can be rewritten to give the following

$$\frac{d\rho}{dt} = \frac{\rho_0 - \rho}{\tau_r} - \frac{\sigma}{\eta_c(\rho)}\rho \tag{13}$$

where k_{diss} has been replaced by $1/\tau_r$, and $\rho_0 = k_{app}\tau_r$, and $\dot{\gamma}$ has been replaced by σ/η_c. For our networks, the effective viscosity, η_c, is dependent on the filament density (through l_c) so this dependence must be included. Solving this equation for its steady states, and replacing the initial density, ρ_0, with the length density approximation, $2/l_c$, we find that a constant steady state density only exists under the condition $\tau_r < \tau_{crit} = \eta_c/2\sigma$.

Reducing recycling time, τ_r, below τ_{crit} produced different effects on steady state deformation rates depending on the relative values of τ_r and τ_c, the characteristic time for the transition to effectively viscous deformation in the absence of recycling. For $\tau_r > \tau_c$, the effective viscosity remained ∼constant with decreasing τ_r; for $\tau_r < \tau_c$, effective viscosity decreased sublinearly with decreasing τ_r. The intuitive explanation for this is as follows: For $\tau_r > \tau_c$, the deformation rate is dominated by cross-link resistance to sliding of strained filaments. For $\tau_r < \tau_c$, the deformation rate is limited by the level of elastic stress on partially strained filaments; By replacing partially strained with unstrained filaments, the network is able to tune the mean level of stress and thus the deformation rate.

To confirm this relationship more generally, we allowed filament lengths, network density and cross link friction to vary more widely, and we measured the network
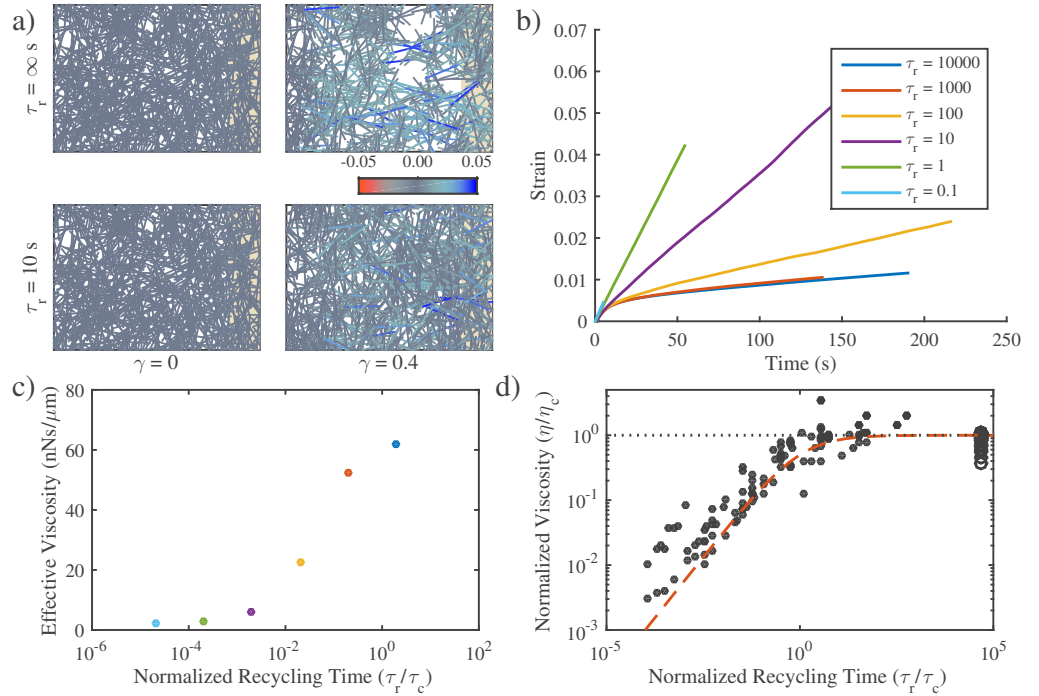
Figure 4. Filament recycling modulates effective viscosity in two regimes. **a)** Examples of $20 \times 12\mu m$ network under 0.001 $nN/\mu m$ extensional stress with recycling ($\tau_r = 10s$) and without, ($\tau_r = \infty$). Both images are taken when the patches had reached a net strain of 0.4. The network with recycling doesn't appear to change shape because its components have been recycled to remain in the original domain. Network parameters: $L = 3\,\mu m$, $l_c = 0.5\,\mu m$, $\xi = 10\,nN \cdot s/\mu m$. **b)** Strain curves for identical networks with varying levels of filament recycling. Network parameters: $L = 3\,\mu m$, $l_c = 0.5\,\mu m$, $\xi = 10\,nN \cdot s/\mu m$. **c)** Plotting the effective viscosity derived from the slopes of the lines in panel a. **d)** Effective viscosities (normalized by the effective viscosity in the absence of recycling, η_c) as a function of the normalized recycling time. When the recycling timescale is significantly less than the passive relaxation timescale, the viscosity of the network becomes dependent on recycling time. Red dashed line indicates the approximation given in equation 14 for $m = 3/4$.

deformation rates while varying filament recycling times (Figure 4a,b). We then plotted the normalized effective viscosity (ratio of effective viscosity with recycling to effective viscosity without recycling, η_c) vs a normalized recycling rate (recycling time scaled by τ_c). Indeed, we found that the normalized effective viscosity measured during steady state flow begins to decrease when the recycling time falls below τ_c and below this value the effective viscosity falls off nearly linearly with recycling time to minimal values (Figure 4c).

To describe this we introduce (based on linear viscoelastic models of [McCrum et al., 1997]) an effective recycling viscosity, η_r, which can be tuned between the τ_r dependent and independent regimes, depending on the value of the recycling timescale.

$$\eta_r = \frac{\eta_c}{1 + (\tau_c/\tau_r)^m} \tag{14}$$

For $\tau_r \gg \tau_c$, this simplifies to $\eta_r \approx \eta_c$, while for $\tau_r \ll \tau_c$, this simplifies to $\eta_r \sim (\tau_r/\tau_c)^m$, which matches with our measurements as found in Figure 4d for a large range of parameters (with $m = 3/4$). While we don't have a clear understanding of the

origins of the 3/4 scaling, this model presents a simple quantitative description of our simulation data.

In summary, we find that tuning recycling times below a critical value τ_{crit}, allows networks to undergo continuous viscous deformation, for long times, without tearing, for a wide range of different effective viscosities and deformation rates. Given a suitably low strain rate, τ_{crit} will be substantially larger than the other timescales of interest. For $\tau_r < \tau_{crit}$, modulating filament recycling times can furthermore tune the network between two regimes. For $\tau_r > \tau_c$, the deformation is limited by effective cross-link friction. The effective viscosity depends on the strength of inter-filament cross-linking and the network's architecture, and is relatively insensitive to changes in recycling rate. For $\tau_r < \tau_c$, the deformation is governed by the buildup of elastic stress on network filaments, and effective viscosity becomes strongly dependent on recycling time.

These findings are in agreement with previous simulations on effective viscosity in cross-linked networks. A previous analysis [Kim et al., 2014] looked at the effect of a different form of filament turnover in networks with irreversible cross-linking. The authors also showed two regimes of deformation: one in which network deformation was linearly viscous and tuned by the turnover rate, and one where the creep rate was set purely by the turnover rate independent of applied force. Although the implementation is different, the two regimes observed in our model are in qualitative agreement and arise from similar microscopic origins. Specifically, the short recycling time regime, where the mechanics are governed by filament extension, is directly equivalent in both models. For this regime, our model is able to give a theoretical description of the effective viscosity found in [Kim et al., 2014]. For the opposite regime of long recycling times, the models have a distinct difference. For the model of [Kim et al., 2014] there was no cross-link unbinding so without of filament turnover, the network would not deform beyond its elastic limit. In contrast, our simulations always require non-zero cross-link slip so there is always some viscous network deformation. Therefore, in the regime of long recycling times our model approaches the limit of cross-link dominated viscosity whereas the model of [Kim et al., 2014] approached an infinite viscosity limit.

Filament recycling allows persistent stress buildup in active networks

In the absence of filament recycling, active networks with free boundaries contract and then stall against passive resistance to network compression. Previous theoretical and experimental studies [Lenz et al., 2012, Murrell and Gardel, 2012, Koenderink et al., 2009] identified asymmetric filament compliance and dispersion in motor force as minimal requirements for contraction of disordered networks. To test if our simple implementation of these two requirements (see Models section) was sufficient to produce macroscopic contraction, we simulated active networks that were unconstrained by external attachments. Turning on motor activity in an initially unstrained network at $t = 0$ produced a rapid initial contraction, followed by a progressive buildup of elastic stress due to compression of individual filaments and an $\sim$exponential approach to stall (Figure 5). The time to stall, τ_s, scaled as $L\xi/\upsilon$ (see S4 Figb), although the origins of this scaling relationship remain unclear. On a longer timescale, polarity sorting of individual filaments, as previously described [Nedelec et al., 1997, Surrey et al., 2001] rearranged the entire network, undoing the initial contraction (see S2 Video).

We focus here on the contraction phase. During the rapid initial contraction, bulk network strain matched closely the mean compressive strain on individual filaments Figure 5b, confirming that the origin of bulk contraction in our simulations is filament buckling due to asymmetric filament compliance, as predicted by [Lenz et al.,
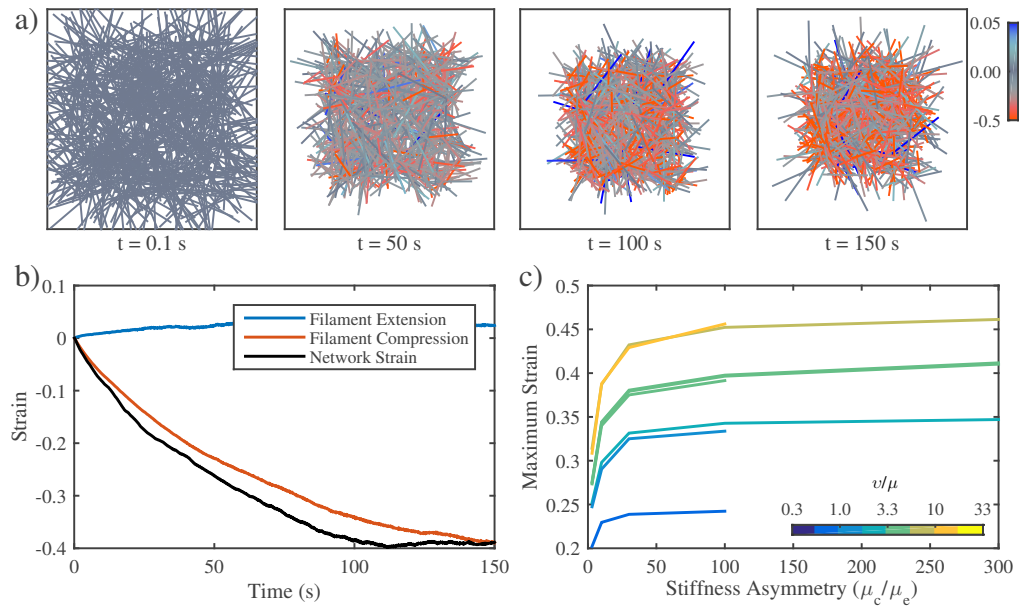
Figure 5. In the absence of filament recycling, active networks with free boundaries contract and then stall against passive resistance to network compression. **a)** Example of an active network contracting. Note the buildup of compressive stress as contraction approaches stall between 100 s and 150 s. Network parameters: $L = 5\,\mu m$, $l_c = 0.3\,\mu m$, $\xi = 100\,nN \cdot s/\mu m$, $\upsilon = 0.1\,nN$. **b)** Plots showing time evolution of total network strain and the average extensional (blue) or compressive (red) strain on individual filaments. **c)** The network's ability to deform relies on the magnitude of asymmetric filament compliance. Total network strain also increases with the applied myosin force υ. Note that the extent of contraction approaches an asymptotic limit as the stiffness asymmetry approaches a ratio of ~ 100.

2012, Lenz, 2014] and observed experimentally [Murrell and Gardel, 2012]. Contraction only occurred when the fractional motor activity $0 < \phi < 1$ (i.e. the fraction of filament intersections with active motors) was less than one, confirming the requirement for dispersion of motor activity (see S4 Fig). Thus, our model effectively captures a minimal mechanism for bulk contractility in disordered networks through asymmetric filament compliance and dispersion of motor activity.

We also determined how microscale parameters shape the rate and final extent of network contraction. Consistent with the idea that contraction stalls when the elastic resistance to filament compression balances the contractile stress., the final extent of contraction increased sharply with motor activity (υ) and with the asymmetry in filament stiffness (i.e. the ratio of the extensional and compressive stiffnesses μ_e/μ_c, Figure 5c,

Active networks can only exert a transient stress against a fixed boundary in the absence of filament recycling. The previous results reveal internal limits on the contraction of networks with free boundaries. However networks typically build force and contract against an external resistance. Therefore, we analyzed the buildup and maintenance of contractile stress in active networks contracting against a rigid boundary. We simulated active networks contracting from an initially unstressed state against a fixed boundary (Figure 6a), and monitored the time evolution of mean extensional (blue), compressional (red) and total (black) stress on network filaments
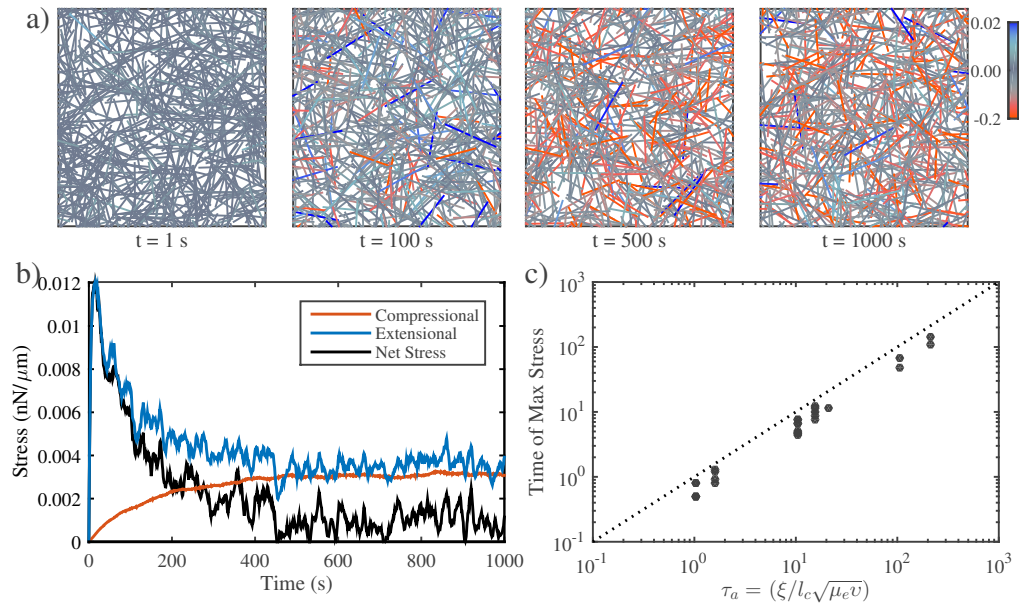
Figure 6. In the absence of filament recycling, active networks can only exert a transient force against a fixed boundary. **a)** Simulation of an active network with fixed boundaries illustrating progressive buildup of internal stress through local filament rearrangement and deformation. Note the progressive buildup of compressive stress on individual filaments. Network parameters: $L = 5\,\mu m$, $l_c = 0.3\,\mu m$, $\xi = 100\,nN \cdot s/\mu m$, $v = 0.1\,nN$. **b)** Plots of total network stress and the average extensional (blue) and compressive (red) stress on individual filaments for the simulation shown in (a). Rapid buildup of extensional stress allows the network transiently to exert force on its boundary, but this force is dissipated at longer times as internal extensional and compressive stresses become balanced. **c.** Measurement and prediction of the characteristic time (τ_a) at which the maximum stress is achieved.

(Figure 6b). We observed the same qualitative behavior for all network parameters examined: Total stress built rapidly to a peak value σ_a, and then decayed back to zero again. The initial rise in total stress was driven by a rapid buildup of extensional stress, while the decay was caused by a slower dissipation of extensional stress and a comparably slow buildup of compressional stress.

Sampling these dynamics over a large range of network parameters, we found that the peak stress occurred at a characteristic time, $\tau_a \sim \xi/l_c\sqrt{\mu_e v}$, as shown in Figure 6c. Although, the origins of this peculiar scaling are unclear, the measurement does agree with our intuitive predictions: The time to reach peak stress should vary directly with the cross-link coupling (ξ) and filament density ($2/l_c$), and it should inversely with the square root of both the filament stiffness (μ_e) and motor force (v).

After this period of peak stress buildup, there is a later phase of stress relaxation. We believe this return to 0 net stress at longer times can originate from multiple sources. First, we note that previous work [Mak et al., 2016] has found a form of transient stress generation that relied on network rearrangements over long times to dissipate stress. We believe that this certainly accounts for a large part of the stress dissipation, especially in a region of phase space where large scale deformations occur. However, a second, indirect, mechanism seems to reduce the net stress via the internal buildup of force on compressed filaments to balance the force being exerted by filaments in extension. This effect does not truly dissipate internal stress, but rather balances the compressive and

extensional stresses such that the net exerted stress cancels out. Because the buildup of internal stress is dependent on the will necessarily take place on a longer timescale than τ_a. In addition, a preliminary analysis has revealed that the internal buildup of stress appears to always take place over a time period longer than the previously derived timescale of free contraction stalling τ_s. This makes sense as the contraction against no resistance should necessarily act as a lower bound to the timescale of contraction against the resistance of filaments that have been constrained by periodic boundary conditions.

At any rate, these multiple timescales ultimately work together to make a clear derivation of the timescale of stress decay more complex than the timescales derived up to now in this work. However, for the time being, we use the inequality $tau_a < \tau_s$ derived from the physiological estimates found in Table 1, along with our preliminary observation that the timescale of stress dissipation is longer than τ_s to constrain our attention to the region of phase space where stress builds up on some timescale τ_a and decays on some longer, unknown timescale. A careful analysis of the interplay of all of these multiple timescales will need to be set aside to focus on the more physiologically relevant details under this situation.

Filament recycling allows networks to exert sustained stress on a fixed boundary. To explore how this limitation could be relieved by filament recycling, we considered an active network contracting against a fixed boundary, using the same parameters as in Figure 6, and systematically varied filament recycling rates. Adding filament recycling produced two general effects: First, as for the passive case, filament recycling could prevent catastrophic tearing by continuously repairing local structural heterogeneities, and by steadily opposing the effects of local strain thinning (see S3 Fig). Second, we found that filament recycling resulted in biphasic modulation of the level of steady state stress.

For the same network parameters as in Figure 7a and slow filament recycling ($\tau_r = 1000s$), the network stress peaked rapidly, but then relaxed to a lower value that persisted for times much longer than τ_a. Decreasing recycling time produced a sharp increase in the steady state stress, although the steady state stress remained lower than its peak value. However, further decreases in recycling time lead to decreases in the steady state stress as well as sharp decreases in the peak stress. Intuitively, this bimodal dependence of steady state stress on recycling rates emerges from continuous replacement of strained with unstrained filaments, combined with the different timescales for buildup of extensional vs compressive filament stress (Figure 7b). Because extensional stress builds more rapidly than compressive stress, lowering the recycling time τ_c should increase net stress until τ_c is approximately equal to τ_a, the time required to build peak stress from an initially unstressed state. For shorter recycling times, the average filament will not have time to build maximum extensional stress before turning over, and thus the steady state stress should decrease with further decreases in τ_c. Plotting normalized steady state stress (steady state stress/peak stress) vs normalized recycling time (τ_c / τ_a) confirms that this biphasic dependence of steady state stress on recycling times holds for a large range of sampled values for network parameters 7d.

In the same manner as for the equation of passive response (i.e. Equation 14), we can approximate the dependence of the steady state stress on the filament recycling rate using a simple equation.

$$\sigma_{ss} = \frac{\sigma_{peak}}{(\tau_r/\tau_a)^n + \tau_a/\tau_r} \quad (15)$$

For $\tau_r \gg \tau_a$, this simplifies to $\sigma_{ss} \sim (\tau_a/\tau_r)^n$, while for $\tau_r \ll \tau_a$, this simplifies to $\sigma_{ss} \sim \tau_r/\tau_a$. What sets the scaling n remains unclear, and this scaling does not appear to be consistent across all simulation setups (Figure 7d). However, equation 15 still captures a qualitatively correct description of steady state stress in our simulation data.
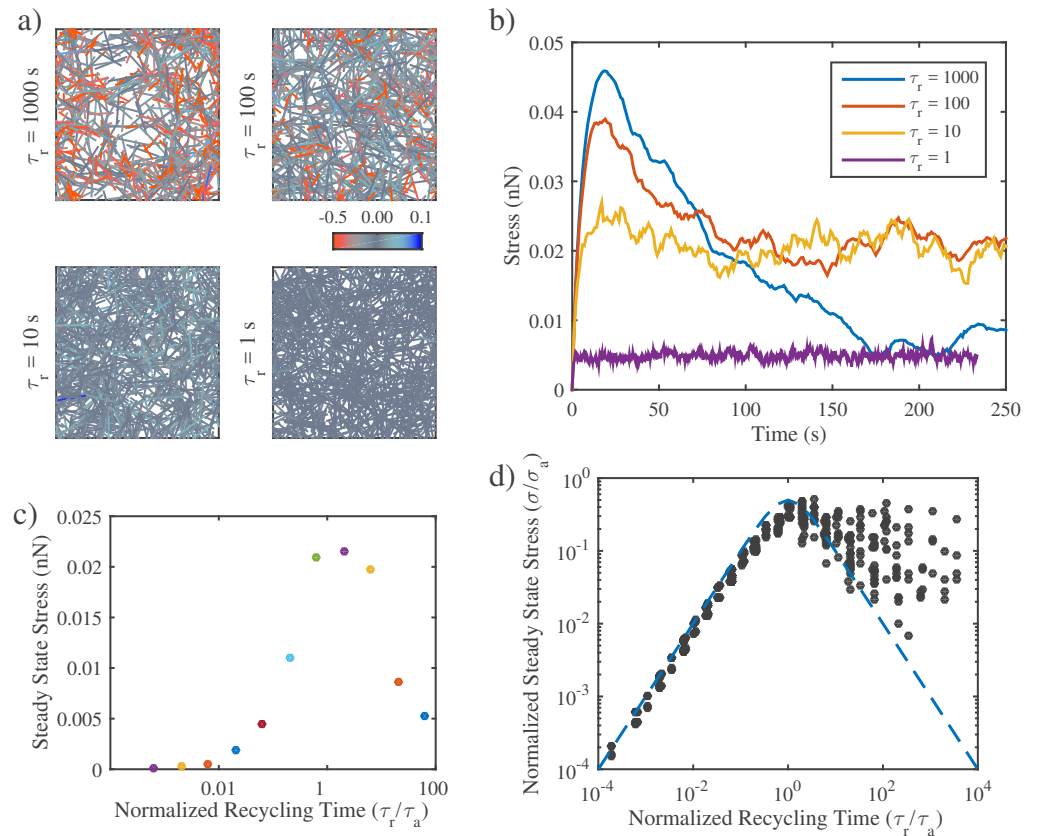
Figure 7. Filament recycling allows network to exert sustained stress on a fixed boundary. **a)** Snapshots from simulations of active networks with fixed boundaries for different timescales of filament recycling. Network parameters are the same as in Figure 6. Note that significant remodeling occurs for longer recycling times. **b)** Plots of net stress exerted by the network on its boundaries for different recycling times; for long-lived filaments, stress is built rapidly, but then dissipates. Increasing filament turnover rates reduces stress dissipation by recycling compressed filaments; however, very short recycling times prevent any stress from being built up in the first place. **c)** Plotting the steady state stress derived from the long term stress values of the stress in panel b. **d)** Normalized steady state stress as a function of normalized recycling time. The steady state stress is set by the timescale at which the network strain is refreshed relative to the timescale at which the max stress is reached. The values have been normalized to the predicted peak stress, σ_a in the absence of recycling. Blue dashed line indicates the approximation given in equation 15 for $n = 1$.

Filament recycling tunes the balance between active stress buildup and viscous stress relaxation to generate flows

Thus far, we have characterized how filament recycling tunes effective viscosity during passive deformation in response to an externally applied stress as well as the steady state stress produced by an active network against an external resistance. We next sought to characterize how filament recycling tunes the steady flows produced by gradients of motor activity as regions of high motor activity contract against the passive resistance of a neighboring region with low motor activity.
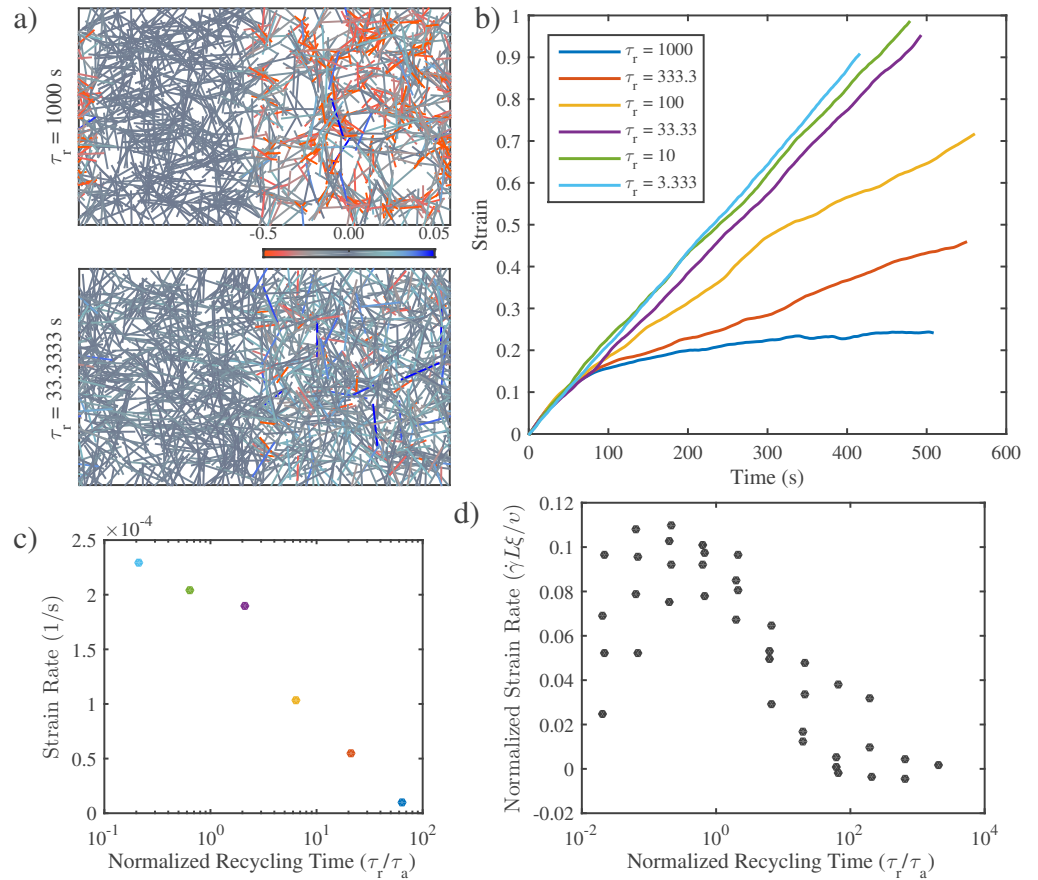
Figure 8. Filament recycling allows sustained flows in networks with non-isotropic activity. **a)** Example simulations of non-isotropic networks with long ($\tau_r = 1000$) and short ($\tau_r = 33$) recycling timescales. In these networks the left half of the network is passive while the right half is active. Network parameters are same as in Figures 6 and 7. Importantly, in all simulations $\tau_a < \tau_c$. **b)** Graph of strain for identical networks with varying recycling timescales. With long recycling times, the network stalls; reducing the recycling timescale allows the network to persist in its deformation. However, for the shortest recycling timescales, the steady state strain begins to slowly return to 0 net motion. **c)** Graph of network long-term strain rate as a function of recycling timescale for simulations in a) and b). **d)** Graph of network long-term strain rate as a function of recycling timescale across a wide range of parameter space. Note that networks only begin to maintain long-term flows when the recycling time is less than $100\tau_a$.

Filament recycling allows sustained flows in networks with non-isotropic 530
activity. We imposed a continuously asymmetric distribution of motor activity on an 531
initially uniformly dense network of passively cross-linked filaments by allowing a 532
fraction of cross links to be active only in the right half of the simulation domain. Then 533
we examined the time-dependent deformation of the network for a range of different 534
filament recycling times Figure 8a. We observed a sharp dependence of steady flow on 535
filament recycling rate Figure 8b,c. For very longer recycling times, ($\tau_r = 1000s$, dark 536
blue line), there was a rapid initial deformation (contraction of the active domain and 537
dilation of the passive domain), followed by a slow approach to a steady state flow 538
characterized by slow contraction of the right half-domain and a matching dilation of 539

the left half-domain (see S6 Fig). However, with decreasing filament recycling times, we found the network was able to largely sustain its deformation and that the long term strain rate remained relatively high (Figure 8c). We repeated these measurements for more network parameters and found that at the shortest recycling timescales measured, we still saw the effective viscosity remaining relatively high, indicating that for short recycling times the effective viscosity may be somewhat buffered against variation in recycling times (Figure 8d).
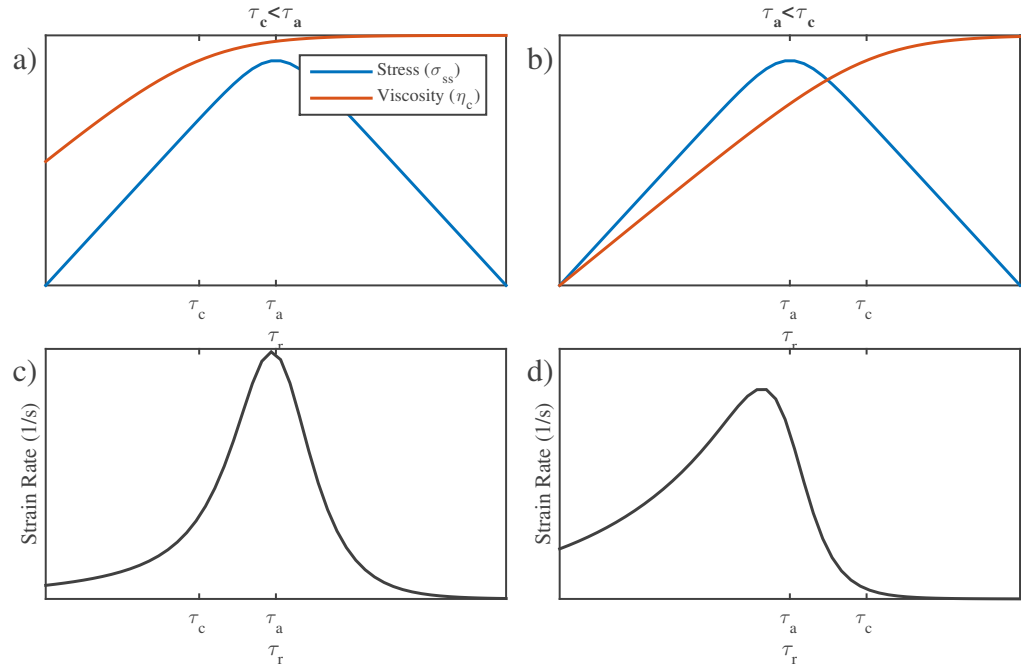

Figure 9. Filament recycling tunes the magnitudes of both effective viscosity and steady state stress. **a)** Dependence of steady state stress and effective viscosity on recycling time τ_r under the condition $\tau_c < \tau_a$. **b)** Same as a), but for the case where $\tau_a < \tau_c$. **c,d)** Resulting strain rates for network as a function of recycling time τ_r for the regimes in panels a and b..

Filament recycling tunes the magnitudes of both effective viscosity and steady state stress. This dependence of steady state deformation (flow) rate on filament recycling times can be understood in terms of our previous findings. During steady state flow, active contraction of the right half-domain is limited both by internal resistance to compression of filaments within the right half-domain (Figure 5), and by passive resistance of the left-half domain (Figure 4).

Monitoring these two forms of resistance as a function of filament recycling time for the simulations in Figure 8, we see that resistance to compression of filaments in the right half domain makes a significant contribution only for very low recycling rates. This is because using physiologically relevant values for network parameters (described above) sets up a condition where compressional resistance on filaments in the contracting right half domain takes longer to build than extensional resistance on filaments in the dilating right half-domain (i.e. $\tau_c < \tau_s$). As a consequence, except for very low recycling rates ($\tau_r > \tau_{crit}$), steady state deformation is governed by an equation of the form:

$$\dot{\gamma} = \frac{\sigma_{ss}}{\eta_r} \tag{16}$$

where σ_{ss} is the active stress generated by the right half-domain (less the internal resistance to filament compression), η_r is the effective viscosity of the left half domain and strain rate is measured in the left half-domain. Therefore, we can understand the dependence of network flow (i.e. strain rate) on filament recycling time τ_r in terms of the previously characterized dependencies of effective viscosity and steady state stress on τ_r (Figures 4d and 7d). In particular, recall that there is a transition in the dependence of η_r on τ_r at the characteristic time τ_c, and a transition in the dependence of σ on τ_r at the characteristic time τ_a. Thus, as shown in Figure 9, there are two qualitatively distinct cases for the dependence of strain rate on τ_r, depending on the relative magnitudes of τ_a and τ_c. For both cases, we expect a decrease in strain rate with filament recycling at long recycling times (where effective viscosity is insensitive to strain rate) and approach to a slowly varying strain rate at low recycling times, where both η_r and σ_{ss} fall off with different scalings. For $\tau_a < \tau_c$, we predict a peak strain rate at intermediate recycling times followed by a rapid falloff at lower recycling times, whereas for $\tau_a > \tau_c$, we expect a more rapid approach to maximum strain rate and a slower fall off at lower recycling times. As shown in Figure 9d, for the range of network parameters we sampled, the strain rate rapidly increases as τ_r is lowered towards τ_a and then more slowly decays to 0 as τ_r is further decreased. This is to be expected because all the parameter values sampled (selected for physiological relevance) satisfied the condition $\tau_a > \tau_c$.
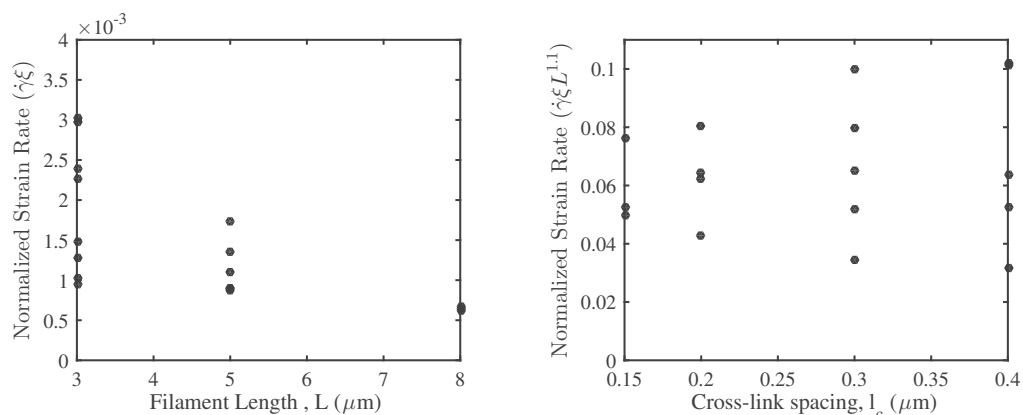

Figure 10. Filament recycling influences architectural control of flow rate. **a)** For a fixed filament recycling time, filament length tuned network deformation rate. **b)** Recycling rate is independent of cross-link spacing in this parameter space.

Filament recycling influences architectural control of flow rate. Finally, we examined how steady state flow depends on other network parameters when filament recycling rates are held constant. Interestingly, we found that flow rates are largely insensitive to cross link density (l_c) but vary inversely with filament length. Thus, in this region of parameter space, steady state flows may be buffered intrinsically against some forms of variation in network architecture.

Conclusion

Our work aimed to create a simulation framework that would allow us to analyze the origins of macroscopic flow in terms of a handful of physiologically relevant microscopic parameters. Toward this aim we developed a minimalist model of a 2D filament network and analyzed the network's reaction to a variety of situations. We found mathematical

relationships that determined both the passive effective viscosity and the active stress generation of networks with and without recycling. From these relationships we were able to make predictions about the rates of network flow in non-isotropic networks mimicking those found in polarized eukaryotic actomyosin cortices.

Importantly, our work brings a theoretical understanding to the importance of actomyosin turnover in producing and maintaining long-term large scale flows. We propose the concept of "filament recycling" to refer to the multitude of biochemical interactions which can give rise to the piece by piece architectural resetting of filament networks. We believe that our analysis of networks in the presence of this filament recycling will be useful in further developing the qualitative and quantitative understanding the deformation of these complex networks.

Supporting Information

S1 Text. **Bold the title sentence.** Add descriptive text after the title of the item (optional).

S1 Fig. **Bold the title sentence.** Add descriptive text after the title of the item (optional).

S2 Fig. **Mechanical properties of passive networks. a)** Elastic modulus of networks. Our measurements closely match prediction of $G_0 \sim \mu/l_c$. **b)** Placeholder for inevitably another figure relevant to passive properties..

S3 Fig. **Mechanical properties of active networks** Add descriptive text after the title of the item (optional).

S4 Fig. **Mechanical properties of active networks** Add descriptive text after the title of the item (optional).

S6 Fig. **Spatial velocity profile of networks containing passive and active domains.**

S1 Table. **Parameter values.** List of parameter values used for each set of experiments.

S1 Video. **Extensional strain in passive networks.** Movie of simulation setup shown in Figure 2

S2 Video. **Active networks contracting with free boundaries.** Movie of simulation setup shown in Figure 5

Acknowledgments

References

Alvarado et al., 2013. Alvarado, J., Sheinman, M., Sharma, A., MacKintosh, F. C., and Koenderink, G. H. (2013). Molecular motors robustly drive active gels to a critically connected state. *Nat Phys*, 9(9):591–597.

Banerjee and Marchetti, 2011. Banerjee, S. and Marchetti, M. C. (2011). Instabilities and oscillations in isotropic active gels. *Soft Matter*, 7:463–473.

Banerjee et al., 2011. Banerjee, S., Marchetti, M. C., and Müller-Nedebock, K. (2011). Motor-driven dynamics of cytoskeletal filaments in motility assays. *Phys. Rev. E*, 84:011914.

Bausch et al., 1998. Bausch, A. R., Ziemann, F., Boulbitch, A. A., Jacobson, K., and Sackmann, E. (1998). Local measurements of viscoelastic parameters of adherent cell surfaces by magnetic bead microrheometry. *Biophysical Journal*, 75(4):2038 – 2049.

Bois et al., 2011. Bois, J. S., Jülicher, F., and Grill, S. W. (2011). Pattern formation in active fluids. *Phys. Rev. Lett.*, 106:028103.

Bray and White, 1988. Bray, D. and White, J. (1988). Cortical flow in animal cells. *Science*, 239(4842):883–888.

Broedersz et al., 2010. Broedersz, C. P., Depken, M., Yao, N. Y., Pollak, M. R., Weitz, D. A., and MacKintosh, F. C. (2010). Cross-link-governed dynamics of biopolymer networks. *Phys. Rev. Lett.*, 105:238101.

Broedersz et al., 2009. Broedersz, C. P., Storm, C., and MacKintosh, F. C. (2009). Effective-medium approach for stiff polymer networks with flexible cross-links. *Phys. Rev. E*, 79:061914.

Chandran and Mofrad, 2010. Chandran, P. L. and Mofrad, M. R. K. (2010). Averaged implicit hydrodynamic model of semiflexible filaments. *Phys. Rev. E*, 81:031920.

Chugh et al., 2016. Chugh, P., Clark, A. G., Smith, M. B., Cassani, D. A. D., Charras, G., Salbreux, G., and Paluch, E. K. (2016). Nanoscale organization of the actomyosin cortex during the cell cycle. *Biophysical Journal*, 110(3):198a.

Dierkes et al., 2014. Dierkes, K., Sumi, A., Solon, J., and Salbreux, G. (2014). Spontaneous oscillations of elastic contractile materials with turnover. *Phys. Rev. Lett.*, 113:148102.

Evans and Yeung, 1989. Evans, E. and Yeung, A. (1989). Apparent viscosity and cortical tension of blood granulocytes determined by micropipet aspiration. *Biophysical Journal*, 56(1):151–160.

Filippov et al., 2004. Filippov, A. E., Klafter, J., and Urbakh, M. (2004). Friction through dynamical formation and rupture of molecular bonds. *Phys. Rev. Lett.*, 92:135503.

Head et al., 2003. Head, D. A., Levine, A. J., and MacKintosh, F. C. (2003). Deformation of cross-linked semiflexible polymer networks. *Phys. Rev. Lett.*, 91:108102.

Heisenberg and Bellaïche, 2013. Heisenberg, C.-P. and Bellaïche, Y. (2013). Forces in tissue morphogenesis and patterning. *Cell*, 153(5):948 – 962.

Hiraiwa and Salbreux, 2015. Hiraiwa, T. and Salbreux, G. (2015). Role of turn-over in active stress generation in a filament network. *ArXiv e-prints*.

Hird and White, 1993. Hird, S. N. and White, J. G. (1993). Cortical and cytoplasmic flow polarity in early embryonic cells of caenorhabditis elegans. *The Journal of Cell Biology*, 121(6):1343–1355.

Hochmuth, 2000. Hochmuth, R. M. (2000). Micropipette aspiration of living cells. *Journal of Biomechanics*, 33(1):15 – 22.

Keren et al., 2009. Keren, K., Yam, P. T., Kinkhabwala, A., Mogilner, A., and Theriot, J. A. (2009). Intracellular fluid flow in rapidly moving cells. *Nat Cell Biol*, 11(10):1219–1224.

Kim et al., 2014. Kim, T., Gardel, M. L., and Munro, E. (2014). Determinants of fluidlike behavior and effective viscosity in cross-linked actin networks. *Biophysical Journal*, 106(3):526 – 534.

Kim et al., 2011. Kim, T., Hwang, W., and Kamm, R. D. (2011). Dynamic role of cross-linking proteins in actin rheology. *Biophysical Journal*, 101(7):1597–1603.

Koenderink et al., 2009. Koenderink, G. H., Dogic, Z., Nakamura, F., Bendix, P. M., MacKintosh, F. C., Hartwig, J. H., Stossel, T. P., and Weitz, D. A. (2009). An active biopolymer network controlled by molecular motors. *Proceedings of the National Academy of Sciences of the United States of America*, 106(36):15192–15197.

Köhler and Bausch, 2012. Köhler, S. and Bausch, A. R. (2012). Contraction mechanisms in composite active actin networks. *PLoS ONE*, 7(7):e39869.

Lenz, 2014. Lenz, M. (2014). Geometrical origins of contractility in disordered actomyosin networks. *Phys. Rev. X*, 4:041002.

Lenz et al., 2012. Lenz, M., Gardel, M. L., and Dinner, A. R. (2012). Requirements for contractility in disordered cytoskeletal bundles. *New Journal of Physics*, 14(3):033037.

Lieleg and Bausch, 2007. Lieleg, O. and Bausch, A. R. (2007). Cross-linker unbinding and self-similarity in bundled cytoskeletal networks. *Phys. Rev. Lett.*, 99:158105.

Lieleg et al., 2008. Lieleg, O., Claessens, M. M. A. E., Luan, Y., and Bausch, A. R. (2008). Transient binding and dissipation in cross-linked actin networks. *Phys. Rev. Lett.*, 101:108101.

Lieleg et al., 2009. Lieleg, O., Schmoller, K. M., Claessens, M. M. A. E., and Bausch, A. R. (2009). Cytoskeletal polymer networks: Viscoelastic properties are determined by the microscopic interaction potential of cross-links. *Biophysical Journal*, 96(11):4725–4732.

Liu et al., 2007. Liu, J., Koenderink, G. H., Kasza, K. E., MacKintosh, F. C., and Weitz, D. A. (2007). Visualizing the strain field in semiflexible polymer networks: Strain fluctuations and nonlinear rheology of f-actin gels. *Phys. Rev. Lett.*, 98:198304.

Liverpool et al., 2009. Liverpool, T. B., Marchetti, M. C., Joanny, J.-F., and Prost, J. (2009). Mechanical response of active gels. *EPL (Europhysics Letters)*, 85(1):18007.

Mak et al., 2016. Mak, M., Zaman, M. H., Kamm, R. D., and Kim, T. (2016). Interplay of active processes modulates tension and drives phase transition in self-renewing, motor-driven cytoskeletal networks. *Nat Commun*, 7.

Marchetti et al., 2013. Marchetti, M. C., Joanny, J. F., Ramaswamy, S., Liverpool, T. B., Prost, J., Rao, M., and Simha, R. A. (2013). Hydrodynamics of soft active matter. *Rev. Mod. Phys.*, 85:1143–1189.

Mayer et al., 2010. Mayer, M., Depken, M., Bois, J. S., Julicher, F., and Grill, S. W. (2010). Anisotropies in cortical tension reveal the physical basis of polarizing cortical flows. *Nature*, 467(7315):617–621.

McCrum et al., 1997. McCrum, N., Buckley, C., and Bucknall, C. (1997). *Principles of Polymer Engineering*. Oxford science publications. Oxford University Press.

Müller et al., 2014. Müller, K. W., Bruinsma, R. F., Lieleg, O., Bausch, A. R., Wall, W. A., and Levine, A. J. (2014). Rheology of semiflexible bundle networks with transient linkers. *Phys. Rev. Lett.*, 112:238102.

Munro et al., 2004. Munro, E., Nance, J., and Priess, J. R. (2004). Cortical flows powered by asymmetrical contraction transport {PAR} proteins to establish and maintain anterior-posterior polarity in the early c. elegans embryo. *Developmental Cell*, 7(3):413 – 424.

Murrell and Gardel, 2014. Murrell, M. and Gardel, M. L. (2014). Actomyosin sliding is attenuated in contractile biomimetic cortices. *Molecular Biology of the Cell*, 25(12):1845–1853.

Murrell and Gardel, 2012. Murrell, M. P. and Gardel, M. L. (2012). F-actin buckling coordinates contractility and severing in a biomimetic actomyosin cortex. *Proceedings of the National Academy of Sciences*, 109(51):20820–20825.

Nedelec et al., 1997. Nedelec, F. J., Surrey, T., Maggs, A. C., and Leibler, S. (1997). Self-organization of microtubules and motors. *Nature*, 389(6648):305–308.

Robin et al., 2014. Robin, F. B., McFadden, W. M., Yao, B., and Munro, E. M. (2014). Single-molecule analysis of cell surface dynamics in caenorhabditis elegans embryos. *Nat Meth*, 11(6):677–682.

Salbreux et al., 2012. Salbreux, G., Charras, G., and Paluch, E. (2012). Actin cortex mechanics and cellular morphogenesis. *Trends in Cell Biology*, 22(10):536 – 545.

Salbreux et al., 2009. Salbreux, G., Prost, J., and Joanny, J. F. (2009). Hydrodynamics of cellular cortical flows and the formation of contractile rings. *Phys. Rev. Lett.*, 103:058102.

Sanchez et al., 2012. Sanchez, T., Chen, D. T. N., DeCamp, S. J., Heymann, M., and Dogic, Z. (2012). Spontaneous motion in hierarchically assembled active matter. *Nature*, 491(7424):431–434.

Spruijt et al., 2010. Spruijt, E., Sprakel, J., Lemmers, M., Stuart, M. A. C., and van der Gucht, J. (2010). Relaxation dynamics at different time scales in electrostatic complexes: Time-salt superposition. *Phys. Rev. Lett.*, 105:208301.

Surrey et al., 2001. Surrey, T., Nédélec, F., Leibler, S., and Karsenti, E. (2001). Physical properties determining self-organization of motors and microtubules. *Science*, 292(5519):1167–1171.

Turlier et al., 2014. Turlier, H., Audoly, B., Prost, J., and Joanny, J.-F. (2014). Furrow constriction in animal cell cytokinesis. *Biophysical Journal*, 106(1):114 – 123.

Unterberger and Holzapfel, 2014. Unterberger, M. J. and Holzapfel, G. A. (2014). Advances in the mechanical modeling of filamentous actin and its cross-linked networks on multiple scales. *Biomechanics and Modeling in Mechanobiology*, 13(6):1155–1174.

Vanossi et al., 2013. Vanossi, A., Manini, N., Urbakh, M., Zapperi, S., and Tosatti, E. (2013). *Colloquium* : Modeling friction: From nanoscale to mesoscale. *Rev. Mod. Phys.*, 85:529–552.

Wachsstock et al., 1994. Wachsstock, D., Schwarz, W., and Pollard, T. (1994). Cross-linker dynamics determine the mechanical properties of actin gels. *Biophysical Journal*, 66(3, Part 1):801 – 809.

Ward et al., 2015. Ward, A., Hilitski, F., Schwenger, W., Welch, D., Lau, A. W. C., Vitelli, V., Mahadevan, L., and Dogic, Z. (2015). Solid friction between soft filaments. *Nat Mater*, advance online publication:–.

Wilhelm and Frey, 2003. Wilhelm, J. and Frey, E. (2003). Elasticity of stiff polymer networks. *Phys. Rev. Lett.*, 91:108103.

Yao et al., 2011. Yao, N. Y., Becker, D. J., Broedersz, C. P., Depken, M., MacKintosh, F. C., Pollak, M. R., and Weitz, D. A. (2011). Nonlinear viscoelasticity of actin transiently cross-linked with mutant alpha-actinin-4. *Journal of Molecular Biology*, 411(5):1062 – 1071.

Zumdieck et al., 2007. Zumdieck, A., Kruse, K., Bringmann, H., Hyman, A. A., and Jülicher, F. (2007). Stress generation and filament turnover during actin ring constriction. *PLoS ONE*, 2(8):e696.